

# Electric-field-reinforced affinitive electrolytes for highly reversible aqueous zinc metal batteries

Received: 14 May 2025

Accepted: 25 February 2026

Cite this article as: Yang, M., Zhang, B., Duan, A. *et al.* Electric-field-reinforced affinitive electrolytes for highly reversible aqueous zinc metal batteries. *Nat Commun* (2026). <https://doi.org/10.1038/s41467-026-70366-7>

Ming Yang, Bao Zhang, An Duan, Sha Luo, Luyang Ge, Jiaqi Wang, Yuxi Zhang, Yu Feng, Xiao Huang, Yuyang Tang, Jia Yao, Hao Wang, Houzhao Wan & Wei Sun

We are providing an unedited version of this manuscript to give early access to its findings. Before final publication, the manuscript will undergo further editing. Please note there may be errors present which affect the content, and all legal disclaimers apply.

If this paper is publishing under a Transparent Peer Review model then Peer Review reports will publish with the final article.

## **Electric-Field-Reinforced Affinitive Electrolytes for Highly Reversible Aqueous Zinc Metal Batteries**

Ming Yang<sup>1,2</sup>, Bao Zhang<sup>2\*</sup>, An Duan<sup>2</sup>, Sha Luo<sup>2</sup>, Luyang Ge<sup>1</sup>, Jiaqi Wang<sup>2</sup>, Yuxi Zhang<sup>2</sup>, Yu Feng<sup>2</sup>, Xiao Huang<sup>2</sup>, Yuyang Tang<sup>2</sup>, Jia Yao<sup>1</sup>, Hao Wang<sup>1\*</sup>, Houzhao Wan<sup>1\*</sup>, Wei Sun<sup>2\*</sup>

<sup>1</sup>Hubei Key Laboratory of Micro-Nanoelectronic Materials and Devices, School of Integrated Circuits, Hubei University, Wuhan, 430062, PR China.

<sup>2</sup>School of Materials and Energy, University of Electronic Science and Technology of China, Chengdu, 610054, PR China.

E-mail: zhangbao@uestc.edu.cn (B. Zhang), wangh@hubu.edu.cn (H. Wang), houzhaow@hubu.edu.cn (H. Wan), weisun@uestc.edu.cn (W. Sun).

## Abstract

Aqueous Zn metal batteries offer a safe, low-cost route to grid-scale energy storage yet suffer from dendrite growth and corrosion issues. Conventional electrolyte designs largely overlook electric-field-driven interfacial dynamics such as solvation structure evolution and component redistribution during operation. Here, we propose an affinitive additive strategy featuring high donor number and dipole moment, exemplified by N,N-dimethylurea (DMU), to dynamically modulate Zn<sup>2+</sup> solvation and the structure of the electric double layer under operational electric fields. Guided by physically grounded molecular descriptors, we identify additives capable of electric-field-induced interfacial enrichment, during which strong dipole-field coupling promotes their incorporation into the Zn<sup>2+</sup> solvation shell and promotes more uniform Zn deposition. As a result, the optimized electrolyte achieves a coulombic efficiency of ~99.9% for Zn plating/stripping with only 2 wt% additive. It also sustains stable operation for 700 h at 60% depth of discharge, outperforming the baseline electrolyte. Descriptor-guided screening further reveals that other candidates follow the same pattern, suggesting broader applicability of this approach. Practical Zn||ZnI<sub>2</sub> full cells with high areal capacity (~3 mAh cm<sup>-2</sup>) and low N/P ratio (~1.8) achieve 750 stable cycles at 0.15 A g<sup>-1</sup> with 84.5% capacity retention.

## Introduction

Aqueous batteries, with their intrinsic safety, low cost, and environmental compatibility, have emerged as viable alternatives for large-scale electrical energy storage<sup>1-3</sup>. In particular, Zn metal batteries (ZMBs) combine low redox potential, high theoretical capacity, and the use of abundant raw materials, making them attractive candidates for grid-scale storage<sup>4</sup>. Nevertheless, the thermodynamic instability of Zn in aqueous electrolytes promotes persistent parasitic hydrogen evolution reactions (HER) and corrosion during plating/stripping cycles. As a result, these irreversible side reactions degrade coulombic efficiency (CE) and severely undermine the cycle life essential for practical applications<sup>5,6</sup>. Besides, Zn negative electrodes also suffer from dendritic growth, a common issue with metal negative electrodes. Consequently, addressing the fundamental negative-electrode-related challenges in ZMBs remains a critical hurdle for commercialization.

Electrolyte engineering has emerged as a powerful strategy for mitigating the interfacial irreversibility of Zn metal negative electrodes<sup>7-9</sup>, particularly in aqueous systems where dendrite growth, hydrogen evolution, and parasitic corrosion are prevalent. By modulating Zn<sup>2+</sup> coordination environments and interfacial ion distributions, solvation structure tailoring<sup>10-14</sup> and electric double layer (EDL) engineering<sup>15,16</sup> have enabled notable improvements in reversibility and cycling stability. However, these advances remain constrained by inherent trade-offs. Dilute electrolytes offer insufficient interfacial regulation due to excessive water activity, while highly concentrated systems introduce challenges including elevated viscosity, sluggish ion transport, and increased cost<sup>17,18</sup>. In parallel, many formulations rely on high loadings of organic co-solvents (>10 wt%)<sup>19</sup>, which compromise safety margins and scale-up viability. These limitations reflect a broader conceptual gap: most existing strategies assume static solvation and interfacial behavior and depend on empirical additive screening without accounting for the dynamic electric field environment that governs real-time interfacial processes during operation. A critical yet often overlooked factor underlying these limitations is the dynamic nature of the electrode-electrolyte

interface. In practical operation, intense interfacial electric fields, ranging from  $10^5$  to  $10^7 \text{ V cm}^{-1}$ ,<sup>20,21</sup> continuously modulate the spatial distribution of ions and solvent molecules, dynamically reshaping  $\text{Zn}^{2+}$  solvation shells and interfacial composition. These field-driven perturbations profoundly impact nucleation behavior, surface reactivity, and additive functionality, yet remain largely unaddressed in conventional electrolyte design. Incorporating this dynamic perspective could provide a foundation for rational additive selection, particularly for systems engineered to respond to operational electric fields in situ.

In this work, we report an affinitive additive design for improved reversibility in aqueous ZMBs. Specifically, these affinitive additives combine high donor number (DN) and dipole moment ( $\mu$ ), enabling dual functionality: high-DN molecules engage in stronger coordination interactions with  $\text{Zn}^{2+}$ , while high- $\mu$  imparts strong electric-field-responsiveness. Unlike prior cosolvent engineering strategies, our framework explicitly treats the electrode's interfacial electric field as an active driver of additive migration and adsorption, rather than a passive environment. A combination of experimental and computational methods revealed that under operational polarization, these additives dynamically redistribute to the electric double layer, modulating  $\text{Zn}^{2+}$  solvation environments. We further establish DN and  $\mu$  as practical molecular-level descriptors that predict field-responsive enrichment, providing a generalizable selection rule. Building on this descriptor framework, we performed a high-throughput computational-experimental screening to identify additional molecules that satisfy DN- $\mu$  criterion, further supporting the broader applicability of this design approach. When incorporated into a  $\text{ZnSO}_4$  electrolyte (BE), this electric-field-reinforced affinitive electrolyte (ERAE) exhibits rapid interfacial accumulation of additives, modulating the  $\text{Zn}^{2+}$  solvation shell and markedly extending negative electrode lifespan. ERAE(DMU) achieves a Zn plating/stripping CE of 99.9% and demonstrates high compatibility with diverse positive electrode materials such as  $\text{V}_6\text{O}_{13}$  and  $\text{ZnI}_2$ , enabling stable full-cell cycling at high mass loadings.

## Results

## Design principles of additives

Achieving effective interfacial regulation at low additive concentrations relies on a clear mechanistic understanding of  $\text{Zn}^{2+}$  solvation and its interplay with interfacial electric fields. To this end, we begin by examining how  $\text{Zn}^{2+}$  interacts with its surrounding environment, as the solvation structure strongly influences ion transport and deposition behavior<sup>13</sup>. In aqueous ZMBs,  $\text{Zn}^{2+}$  functions as a Lewis acid that coordinates with solvent molecules or additives containing lone-pair electrons. Molecules with high DN donate electron density more efficiently to  $\text{Zn}^{2+}$ ,<sup>22,23</sup> forming stable coordination complexes that enable co-migration under an applied electric field<sup>24,25</sup>. Meanwhile, species with larger  $\mu$  exhibit strong dipole-field interactions, allowing them to align under electric fields and lower interfacial free energy, which enhances their adsorption<sup>26</sup>. Guided by this dual-parameter principle, we constructed a molecular library spanning a wide range of DN and  $\mu$  values, and evaluated each candidate's interfacial behavior under realistic field conditions. As shown in Figure 1a, we identified three types of additive response: electric-field-weakened shielding electrolytes (EWSE) with low  $\mu$  cannot compete with water for interfacial adsorption; electric-field-weakened inert electrolytes (EWIE) with low DN lack coordination ability and fail to migrate; ERAE with both high DN and  $\mu$  tend to exhibit strong co-migration and sustained interfacial retention.

To systematically assess the effectiveness of additive-induced interfacial regulation, we screened 12 additives spanning a broad range of DN,  $\mu$ , the adiabatic ionization energies (AIEs) and adiabatic electron affinities (AEAs), each introduced at a fixed loading of 2 wt% (Figures S1, S2 and Table S1). Electrochemical Zn plating/stripping tests were conducted using  $\text{Zn}||\text{Zn}$  symmetric cells under harsh conditions (60  $\mu\text{L}$  electrolyte, 60% depth of discharge (DOD); Figure S3), which ensured that observed performance differences could be primarily attributed to interfacial effects. We found that Zn plating/stripping duration correlated strongly and reproducibly with the combined DN- $\mu$  descriptor, supporting the predictive value of our design approach (Figures S4-S6). Interestingly, neither DN nor  $\mu$  alone showed clear correlation with

stability, nor did other common properties (Figure S7). This observation reinforces the importance of jointly considering both DN and  $\mu$  when selecting affinitive additives. We further refined our analysis by employing a machine learning approach to identify the optimal feature pair (Figure 1b and Table S2). Twelve features, including dipole moment, dielectric constant, donor number, ET, and total polar surface area, were selected to generate 66 unique feature pairs. Utilizing Leave-One-Out Cross-Validation (LOOCV) with Ridge regression, we assessed each pair's performance. The DN- $\mu$  combination yielded the lowest root mean square error, identifying it as a robust descriptor pair for predicting additive efficacy.

As shown in Figure 1c, the Zn plating/stripping duration achieved at 60 % DOD is plotted against each additive's DN and  $\mu$ , with bubble size representing performance. Additives located in the upper-right quadrant, combining both high DN and high  $\mu$ , generally achieved lifetimes exceeding 200 hours, reflecting strong interfacial enrichment and stabilization even at low concentration. In contrast, additives with low  $\mu$  are displaced by water at the interface, while those with low DN lacked the coordination ability needed for co-migration with  $\text{Zn}^{2+}$ . As a result, neither class improved negative electrode lifetime relative to the BE, and in several cases, even reduced it. Conversely, ERAE showed clear improvements in Zn plating/stripping duration. This overall trend, mapped against molecular descriptors, highlights the utility of the DN- $\mu$  design framework. Based on these results, ERAE(DMU) and ERAE(MF) emerged as the potential candidates (Figure S8), both extending the Zn plating/stripping duration (Figure S5). Among them, DMU was selected as the principal focus for subsequent studies because it combines strong electrochemical performance with practical advantages in terms of safety and sustainability.

### **Electric-field-induced EDL reconfiguration**

To gain deeper insights into the reconfiguration of the electric double layer (EDL) under applied electric fields, we conducted a comprehensive analysis using in situ electrochemical quartz crystal microbalance (eQCM) coupled with cyclic voltammetry (CV). This technique enables real-time monitoring of additive adsorption and

desorption dynamics at the electrode-electrolyte interface<sup>27</sup>. Three different types of electrolytes were evaluated in 2 m ZnSO<sub>4</sub>. Electrode mass changes were detected via quartz-crystal frequency shifts following the Sauerbrey relation<sup>28</sup>. When paired with CV, this setup enables continuous tracking of interfacial mass variations<sup>29</sup>. Importantly, additives in the ERAE region undergo clear field-driven adsorption/desorption (Figure 2a), as revealed by the combined Pearson-amplitude ratio (AR) analysis in Figures 2b, S9. The Pearson coefficient captures the directional consistency between potential and mass variation, while the AR, extracted from the fundamental oscillation of the mass response, quantifies the strength of electric-field-induced adsorption/desorption. ERAE additives show large negative Pearson values together with high AR, consistent with strong electro-responsiveness. By contrast, EWIE, EWSE, and BE additives exhibit weak correlation and minimal AR values, indicating negligible mass modulation under the applied field. Control QCM measurements on Zn-coated QCM sensors suggest that the observed mass changes are not due to specific chemical adsorption (Figures S10-S12). Based on these observations, we infer that high-DN, high- $\mu$  additives accumulate at the Zn surface under field, leading to the formation of an organic-rich EDL. This is evidenced by a pronounced decrease in electric double-layer capacitance (EDLC) and Mott-Schottky analysis (Figures S13, S14), which reflects the field-driven enrichment of additives. This conclusion is further supported by the reduced Arrhenius activation energy under an applied electric field (Figure S46). To assess the protective effect of this organic-rich EDL, differential electrochemical mass spectrometry (DEMS) was used to monitor H<sub>2</sub> evolution during cycling. Results show that the BE produces consistently higher H<sub>2</sub> levels with intermittent bubble-detachment spikes<sup>19</sup>. In contrast, the ERAE(DMU) substantially reduces gas evolution (Figure 2c). Because the HER is strongly suppressed in ERAE(DMU), fewer byproducts are generated, as confirmed by XRD (Figure S15), and the interfacial passivation layer is correspondingly much thinner, as revealed by XPS depth profiling (Figure S16) and TEM imaging (Figure S17). These results suggest that affinitive additives enrich the EDL and suppress parasitic H<sub>2</sub> evolution.

To further elucidate the electric-field-induced reconfiguration of the EDL at the Zn

electrode interface, we performed constant-potential molecular dynamics (MD) simulations with and without applied bias (Figures 2d, 2e and S18-S20). When an external electric field is applied, DMU molecules accumulate strongly at the interface, demonstrating clear field responsiveness. By contrast, EWIE(SL) shows no field-induced enhancement, with its interfacial distribution remaining nearly unchanged under bias. Quantitative analysis (Figure 2f) further reveals that the surface coverage of ERAE increases markedly under bias, positioning them above the diagonal line, while EWSE and EWIE lie below the line, reflecting their depleted interfacial populations. This field-responsive enrichment suggests that affinitive additives can dynamically reorganize the interfacial environment under electric field, which is associated with reduced parasitic reactions and improved Zn negative electrode stability.

### Interfacial dynamics of $\text{Zn}^{2+}$ solvation shells

The interfacial dynamics of  $\text{Zn}^{2+}$  solvation are also important for efficient additive design. To further elucidate the dynamic modulation of the  $\text{Zn}^{2+}$  solvation shells by ERAE(DMU) under operational electric fields, in situ attenuated-total-reflectance Fourier-transform infrared (ATR-FTIR) spectroscopy was conducted in combination with chronoamperometry to record the time evolution of absolute absorbance,  $[A(t)]$  (Figures S21, S22). In addition, surface-enhanced infrared absorption spectroscopy (SEIRAS) was employed to selectively probe interfacial species with higher sensitivity (Figures S23, S24), thereby complementing the ATR-FTIR analysis. This technique enables real-time monitoring of interfacial chemical environments, providing insights into solvation dynamics during Zn plating and stripping processes<sup>30</sup>. Relative absorbance changes,  $[A(t_x)-A(t_0)]$ , were calculated by subtracting the initial spectrum recorded at  $t_0$ . We then analyzed  $[A(t_x)-A(t_0)]$  over the plating ( $t_0-t_{900}$ ) and stripping ( $t_{900}-t_{1800}$ ) intervals. Notably, the relative absorbance variations closely track the current response, particularly for the O-H stretching vibration [ $\nu_1(\text{H}_2\text{O})$ ] and asymmetric S-O stretching [ $\nu_2(\text{SO}_4^{2-})$ ]. The  $\nu_1(\text{H}_2\text{O})$  includes contributions from both weak (W-H) and strong (S-H) hydrogen bonds. Consistent with previous studies<sup>31</sup>, in the BE,  $\nu_2(\text{SO}_4^{2-})$  absorbance decreases during plating, indicating that  $\text{SO}_4^{2-}$  moves away from the

interface. During stripping,  $\nu_2(\text{SO}_4^{2-})$  absorbance increases, suggesting that  $\text{SO}_4^{2-}$  returns toward the interface. Additionally, hydrogen bonding (HB) in water weakens during plating and strengthens during stripping (Figure 3a). In stark contrast, in the ERAE(DMU), changes in  $\nu_1(\text{H}_2\text{O})$  and  $\nu_2(\text{SO}_4^{2-})$  are markedly suppressed (Figure 3b). SEIRAS demonstrates that ERAE(DMU) undergoes potential-dependent dynamic adsorption and desorption at the electrode surface. This finding indicates that the variations of  $\text{SO}_4^{2-}$  and  $\text{H}_2\text{O}$  observed by in situ ATR-FTIR are instead induced by the interfacial adsorption of ERAE(DMU), highlighting its role in regulating the interfacial environment. These findings suggest that affinitive additives partially exclude both  $\text{H}_2\text{O}$  and  $\text{SO}_4^{2-}$  from the  $\text{Zn}^{2+}$  solvation shell at the interface. These observations are schematically illustrated in Figure 3c, where the dynamic reorganization of  $\text{Zn}^{2+}$  solvation shells under an applied field is depicted.

Subsequently, the interfacial  $\text{Zn}^{2+}$  hydration in ERAE(DMU) and BE was quantified in real time using in situ eQCM during the negative polarization process with carbon black-coated quartz crystals, which allows solvated Zn species to diffuse into the pore structure (Figure S25). The measured  $\Delta m-\Delta Q$  relations were compared with the dotted and dashed theoretical mass, charge slopes corresponding to bare  $\text{Zn}^{2+}$  and fully hydrated  $\text{Zn}^{2+}\cdot 6\text{H}_2\text{O}$ , respectively. In the BE electrolyte, the  $\Delta m-\Delta Q$  plot closely follows the theoretical behavior of the fully hydrated species, and the fitted slope corresponds to an apparent molar mass of  $179 \text{ g mol}^{-1}$  (details of the slope calculation and molar-mass extraction are provided in the Supporting Information). In contrast, the ERAE(DMU) electrolyte exhibits markedly larger mass changes per unit charge, yielding an apparent molar mass of  $202 \text{ g mol}^{-1}$ . These heavier, less-hydrated interfacial Zn complexes suggest that the associative additive may participate in modifying the interfacial solvation environment by partially displacing water molecules from the primary solvation shell of  $\text{Zn}^{2+}$ .

To quantitatively assess the electric-field-responsiveness of molecules in relation to their coordination with  $\text{Zn}^{2+}$ , the binding energy ( $E_b$ ) between each additive and  $\text{Zn}^{2+}$  was calculated as a measure of coordination strength. Electric-field-responsiveness was then evaluated for a series of molecules (Figure 3g). A strong positive correlation

between  $E_b$  and field-responsiveness is observed for ERAE(DMAC, DMSO, DMU, DMF, NMP) indicating both high  $Zn^{2+}$  affinity and pronounced field sensitivity. By contrast, EWSE(MeOH), EWIE(ACN) and  $H_2O$  exhibit weak  $Zn^{2+}$  binding and low field-responsiveness, indicating limited interfacial affinity. As the field strength increases from 0 to  $0.2 \times 10^{-3} \text{ V \AA}^{-1}$ ,  $E_b$  decreases markedly for EWIE(ACN),  $H_2O$ , and EWSE(MeOH) (Figure S26). Among them,  $H_2O$  shows the steepest decline, indicating facile stripping of water ligands under field. In contrast, ERAE(DMAC, DMU, DMF, NMP) exhibit slight increases in  $E_b$ , indicating their resistance to field-induced dissociation and further reinforcement of  $Zn^{2+}$  coordination. This behavior is consistent with field-driven enrichment and stabilization of  $Zn^{2+}$  solvation at the interface. Furthermore, MD simulations were conducted to compare  $Zn^{2+}$  solvation structures under field-free (bulk) and applied-field (interfacial) conditions (Figure 3h). In the absence of bias,  $Zn^{2+}$  solvation is dominated by water molecules, and most additives show negligible participation in the primary solvation shell. Under an applied field, however, ERAE(DMAC, DMF, DMU, DMSO, NMP) partially replace water ligands and become incorporated into the  $Zn^{2+}$  solvation shell, reflecting their strong electric-field responsiveness. By contrast, EWIE (ACN, SL) and EWSE (TAA, TBA) remain largely excluded, indicating little contribution to field-driven solvation restructuring. These results highlight a dual-parameter design principle: additives that combine high  $Zn^{2+}$  binding affinity with strong dipolar response are more likely to accumulate at the interface and actively reorganize  $Zn^{2+}$  solvation under operating conditions.

To rule out bulk effects, ex situ ATR-FTIR, X-ray absorption fine structure (XAFS) and ionic conductivity measurements were performed on both BE and ERAE(DMU). These techniques probe coordination environment, local structure, and transport properties, respectively. ATR-FTIR spectra for BE and ERAE(DMU) (Figure S27) indicates similar  $Zn^{2+}$  coordination environments. Similarly, XANES data (Figure S28) show that the Zn K-edge absorption energies are virtually the same for BE and ERAE(DMU). FT-EXAFS fitting in R space confirms that the first-shell Zn-O coordination is preserved (Figure S29). Wavelet transform analyses (Figures S30, S31) likewise indicate that the local solvation sheath experiences only minimal perturbation.

Together, these results indicate that at 2 wt% additive loading, ERAE(DMU) does not substantially infiltrate bulk  $\text{Zn}^{2+}$  solvation clusters despite their high DN. Moreover, BE and ERAE(DMU) display comparable ionic conductivities (Figure S32), confirming that bulk transport properties remain effectively constant. Therefore, the performance enhancements arise predominantly from interfacial, rather than bulk, additive effects.

### Morphology of deposited Zn

Generally, interfacial  $\text{Zn}^{2+}$  solvation structure plays an important role in governing nucleation behavior<sup>32</sup>, so we next investigated its impact on deposition uniformity. Since electric-field inhomogeneity at the metal-electrolyte interface is known to drive dendritic growth<sup>33</sup>, scanning electrochemical microscopy (SECM) was employed to map the local electric-field distributions across Zn deposit (Figure 4a). Ferrocene methanol (FcMeOH) served as a redox mediator, and its tip current was monitored to report field strength. SECM imaging revealed highly uniform current signals in the ERAE(DMU) (Figure 4b), whereas the BE exhibited distinct inhomogeneity with a depressed region in the center (Figure 4c). This field distortion is associated with uneven  $\text{Zn}^{2+}$  flux, which may promote preferential growth at the electrode edges and symmetry breaking in the nucleation pattern<sup>34</sup>. To observe the dynamic evolution of Zn plating, in situ optical microscopy was performed. The BE system showed increasing surface roughness and visible gas evolution over time, while the ERAE(DMU) exhibited a more compact and uniform deposition front (Figure 4d). Confocal laser scanning microscopy (CLSM) further confirmed these trends, with the BE showing a rougher and more disordered surface compared to the smoother morphology under the ERAE(DMU) (Figure 4e). High-resolution SEM images revealed dense, layered Zn deposits in the ERAE(DMU), in contrast to the porous and irregular structure observed in the BE (Figure 4f). Given that the electro-crystallization rate depends on overpotential and is reflected in current transients, potentiostatic experiments were performed. These measurements were used to probe Zn nucleation and growth kinetics. The resulting  $i-t$  curves (Figure S33) were normalized using the peak current ( $i_m$ ) and corresponding time ( $t_m$ ), and compared with two classical models: the Scharifker-Hills

(SH) model<sup>35</sup> describing 3D diffusion-controlled hemispherical growth (3DI, 3DP), and the Bewick-Fleischmann-Thirsk (BFT) model<sup>36</sup> describing 2D lateral cylindrical growth (2DI, 2DP) (Figure 4g). In the BE, Zn nucleation follows a mixed 2D/3D growth mode. Consequently, 3D growth produces rough, porous deposits that disrupt the uniformity of the Zn plating layer<sup>37</sup>. By contrast, in the ERAE(DMU), Zn deposition is consistent with a predominantly 2DP mode, leading to a smoother, homogeneous layer without pronounced agglomeration.

### Electrochemical performance

Building on the observed interfacial behavior, the electrochemical performance of half cells was further evaluated. The Zn plating/stripping stability of Zn||Zn symmetric cells was assessed at DOD of 30%, 60%, 70%, and 80% using the ERAE(DMU). At 30 % DOD, ERAE(DMU) exhibited a Zn plating/stripping duration of 1625 h; at 60 % DOD, Zn plating/stripping duration was 700 h; at 70 % DOD, 455 h; and at 80 % DOD, 315 h (BE < 100h) (Figure 5a). Furthermore, under a stepwise high-DOD protocol (30%, 60%, 80%, 60%, 30%), the ERAE(DMU) maintained prolonged Zn plating/stripping stability (Figure 5b). Using Aurbach's protocol<sup>38,39</sup> at 60% DOD, Zn CE reached 99.92% in the ERAE(DMU) versus 97.82% in the BE (Figures 5c). CE measurements across all electrolytes (Figures S34-S37) show that ERAE consistently maintains the higher Coulombic efficiency during long-term cycling, indicating enhanced reversibility of Zn plating/stripping behavior. In contrast, EWIE and EWSE display lower reversibility and shorter lifetimes. These results suggest that affinitive additives enhance both Zn negative electrode stability and reversibility, with the improved performance arising from interfacial enrichment that modulates Zn<sup>2+</sup> solvation clusters and promotes a water-deficient EDL. Considering DOD, cumulative plating capacity (CPC), and electrolyte cost, the Zn negative electrode metrics reported here achieve competitive performance (Figure 5d).

Furthermore, positive electrodes compatibility and full-cell performance under harsh conditions were explored. Zn||V<sub>6</sub>O<sub>13</sub> (intercalation-type) full cells were assembled using the ERAE(DMU) to evaluate long-term stability and reversibility. The

galvanostatic charge-discharge (GCD) profiles of the ERAE-based Zn||V<sub>6</sub>O<sub>13</sub> cell at 0.3 A g<sup>-1</sup> (Figure S38) closely match the characteristic V<sub>6</sub>O<sub>13</sub> GCD profiles<sup>40</sup>. The N/P ratio was set to approximately 3. After 900 cycles, the ERAE-based Zn||V<sub>6</sub>O<sub>13</sub> cell retained 87.5% capacity, with an average CE of 98.8% (Figure 6a). In comparison, the BE-based cell retained only 55% of capacity after just 200 cycles and then gradually faded to near zero, without short circuiting. This indicates that parasitic side reactions<sup>41</sup>, rather than dendrite-induced failure, are the dominant cause of capacity loss. These findings suggest that ERAE(DMU) effectively suppresses parasitic reactions and improved Zn negative electrode durability in full cells.

Moreover, Zn||ZnI<sub>2</sub> (conversion-type) full cells were also assembled under high mass loading conditions. GCD profiles at 1 C (0.15 A g<sup>-1</sup>) and 4 C exhibit typical ZnI<sub>2</sub> positive electrode characteristics (Figure S39). Under harsh conditions (E/C ~ 16 μL mAh<sup>-1</sup>, N/P ~ 1.8), the ERAE(DMU) completed 750 cycles at 1 C, retaining 84.5% capacity with an average CE of 99% (Figure 6b). At 4 C rate, the cell sustained 1,000 cycles with 91.5% retention, indicating stable cycling performance and high-rate capability (Figure S40), as well as improved CE. In contrast, the BE showed large CE fluctuations and experienced short circuiting after 130 cycles. This failure is attributed to polyiodide shuttling, which accelerates parasitic reactions at the Zn negative electrode<sup>42</sup> and leads to rapid Zn depletion and dendritic formation. Open-circuit voltage decay tests of fully charged Zn||ZnI<sub>2</sub> cells after 24 h storage show 92.9% capacity retention in the ERAE(DMU), indicating effective suppression of polyiodide shuttling (Figure S41). The ERAE(DMU) also delivers high cumulative discharge capacity (CDC) at low electrolyte cost (Table S6). These results highlight the ability of ERAE(DMU) to stabilize Zn negative electrodes and enable durable, high-performance operation with conversion-type positive electrodes. To assess scale-up feasibility, a Zn||ZnI<sub>2</sub> pouch cell was fabricated using ERAE a 30 mg cm<sup>-2</sup> ZnI<sub>2</sub> positive electrode, a separator, and a 20 μm Zn negative electrode. This configuration yielded an areal capacity of 4 mAh cm<sup>-2</sup>, with an N/P ratio of approximately 3, and a total discharge capacity of 100 mAh for the 25 cm<sup>2</sup> pouch cell. The cell exhibited stable polarization throughout cycling, with only a slight increase compared to the coin cell (Figure 6c).

As a result, a long-term cycling stability of 200 cycles with 99.2% capacity retention was achieved (Figure 6d). Even when paired with MnO<sub>2</sub> positive electrodes, ERAE(DMU) still exhibits enhanced cycling stability and higher CE compared with the BE, demonstrating its broad compatibility with different cathode chemistries (Figures S44, S45). Overall, the electric-field responsiveness of ERAE(DMU) enables stable and efficient cycling performance under demanding full-cell conditions.

### High-throughput screening workflow

To explore the applicability of the DN- $\mu$  design principle beyond the additives experimentally examined in this work, we further developed a high-throughput computational screening pipeline (Figure 7a). Beginning with ~569,000 organic molecules downloaded from PubChem, we applied a sequence of filters based on toxicity, chemical stability, and pH compatibility, narrowing the pool to ~223,000 candidates. Additional constraints related to synthetic accessibility and commercial availability reduced this set to ~20,000 molecules. Efficient xTB calculations were then performed to evaluate three molecular-level criteria informed by our mechanistic understanding: (1) electrochemical stability (AIE > 10.4 eV and AEA < 6.4 eV), (2) high dipole moment (> 5.0 D), and (3) strong Zn-ion binding affinity (0.18 Hartree higher than Zn<sup>2+</sup>-H<sub>2</sub>O interaction).

Application of these criteria yielded ~300 promising candidates (Supplementary Data 1), which were subsequently filtered by cost and commercial accessibility, arriving at ~30 final molecules with DN- $\mu$  characteristics aligned with our design framework. To experimentally interrogate the predictive power of this screening strategy, we selected two inexpensive and commercially accessible additives (piracetam (PIR) and 1-(2-Hydroxyethyl)-2-pyrrolidone (HEP)) from this set and incorporated them into Zn||Zn symmetric cells. As shown in Figure 7b, both additives led to extended Zn plating/stripping duration: ERAE(HEP) achieved a lifetime of 270 h at 60% DOD, while the ERAE(PIR) achieved 615 h under the same conditions. These results provide experimental support for the applicability of our computational design logic.

## Discussion

In this work, an electric-field-reinforced affinitive additive strategy was developed for aqueous Zn metal batteries, leveraging high DN and  $\mu$  to create an electrolyte that dynamically responds to applied fields. Using a suite of in situ techniques (eQCM, ATR-FTIR and SEIRAS) in combination with MD simulations and quantum-chemical calculations, our results indicate that high-DN, high- $\mu$  molecules migrate into the EDL, reorganize field-perturbed  $\text{Zn}^{2+}$  solvation structures, suppress  $\text{H}_2$  evolution, and guide uniform Zn deposition. This leads to stable Zn plating/stripping without evident dendrite formation and achieves a CE of 99.9%. In full cells, the ERAE(DMU)-based  $\text{Zn}||\text{ZnI}_2$  coin cell (N/P  $\sim$  1.8) achieves 750 cycles with 84.5% retention, while the pouch cell (N/P  $\sim$  3) exceeds 200 cycles with 99.2% retention. Beyond a single formulation, the DN- $\mu$  framework was further extended through high-throughput additive screening, suggesting broader applicability and enabling the identification of additional field-responsive candidates. Such dynamic, field-coupled interfacial modulation provides a mechanistic approach to regulating Zn negative electrode behavior while maintaining low additive loading and favorable economic considerations. Moreover, the principle of field-mediated solvation regulation may offer a useful framework for other multivalent battery chemistries that face challenges related to dendrite formation and parasitic reactions. By shifting electrolyte design from bulk-phase optimization toward interfacial field responsiveness, this work highlights the potential of electric-field-affinitive additives in aqueous battery systems.

## Methods

### Chemical reagents

N,N-Dimethylurea (DMU, 98% purity), tert-Butanol (TBA,  $\geq 99\%$  purity), tert-Amyl alcohol (TAA, 99% purity), Methanol (MeOH, 99.5% purity), 1-Methyl-2-pyrrolidinone (NMP,  $> 99.5\%$  purity), N,N-Dimethylacetamide (DMAC, 99% purity), N-Methylformamide (MF, 99% purity), Triethyl phosphate (TEP,  $> 99.5\%$  purity), Piracetam (PIR,  $> 98\%$  purity), 1-(2-Hydroxyethyl)-2-pyrrolidone (HEP,  $> 99.5\%$ ), Ferrocene methanol (FcMeOH, 98% purity) and vanadium pentoxide ( $V_2O_5$ , 99% purity) were purchased from Macklin Biochemical Technology Co. Dimethyl sulfoxide (DMSO,  $> 99.8\%$  purity), N,N-Dimethylformamide (DMF,  $> 99.9\%$  purity) and Sulfolane (SL, 99% purity), Ethylene glycol (EG,  $> 99.5\%$  purity) were purchased from Energy Chemical Co. Zinc sulfate heptahydrate ( $ZnSO_4 \cdot 7H_2O$ ) was purchased from Sinopharm Chemical Reagent Co. Trimethyl phosphate (TMP, 98% purity), Zinc Iodide ( $ZnI_2$ , 99% purity) were purchased from Shanghai Adamas Reagent Co, the gold plating solution was purchased from Shanghai Yuanfang Technology Co., Ltd, The commercial nanoscale  $\alpha$ - $MnO_2$  was purchased from Shanghai Yunfu Nano Technology Co., Ltd. Acetylene black (Kappa 100), CNT-3213, PTFE aqueous dispersion (60 wt%), Ketjen black (EC-600JD) and PVDF 5130 were purchased from Guangdong Canrd New Technology Co.

### Electrolyte preparation

Deionized water was used as the solvent to prepare the aqueous electrolytes. BE (2m  $ZnSO_4$ ) was prepared by dissolving 0.02 mol  $ZnSO_4 \cdot 7H_2O$  in 7.48g of  $H_2O$ . The 2 wt% additive content was calculated based on the total mass of the mixed electrolyte.

### Electrode preparation and cell assembly

$V_6O_{13}$  was prepared as follows<sup>43</sup> (Figure S42, S43). Briefly, 0.9 g of vanadium pentoxide ( $V_2O_5$ ) was dissolved in a mixture of 10 mL of ethanol and 30 mL of DI.

After continuously stirring for 1 h, the solution was transferred to a 50 mL Teflon autoclave and heated at 180°C for 12 h. It was then washed several times with ethanol and dried overnight at 60°C in a vacuum atmosphere to obtain  $V_6O_{13}$ . For  $V_6O_{13}$  free standing positive electrodes, a mixture of active material  $V_6O_{13}$ , acetylene black, CNTs and PTFE binder were pressed in a weight ratio of 7:1:1:1. For  $ZnI_2$  free standing positive electrodes, a mixture of active material  $ZnI_2$ , activated carbon (YEC-8A, Fuzhou Yihuan Carbon Co., Ltd.), and PTFE binder was pressed in a weight ratio of 6:3:1. For  $\alpha$ - $MnO_2$  positive electrodes, a slurry was prepared by mixing  $\alpha$ - $MnO_2$ , Ketjen black, and PVDF binder in a weight ratio of 7:2:1. The slurry was uniformly coated onto 39BB carbon paper (Toray) using a doctor blade, followed by drying overnight at 80 °C. Electrodes were cut into circular disks using a precision puncher. CR2032 coin cells (Guangdong Canrd New Technology Co.) were assembled for electrochemical measurements, maintained at 25°C in a temperature-controlled chamber (Shenzhen Neware Technology Co.).  $Zn||Cu$  cells were assembled by using Zn foil (thickness: 200  $\mu m$ , diameter: 14 mm) as negative electrode and Cu foil (thickness: 20  $\mu m$ , diameter: 19 mm) as positive electrode. Symmetrical cells were assembled by using two Zn foils (thickness: 10  $\mu m$ , diameter: 12 mm). Full cells, including  $Zn||ZnI_2$ ,  $Zn||V_6O_{13}$  were assembled by using thin Zn foil (thickness: 10  $\mu m$ , diameter: 12 mm) as negative electrode and high-loading self-standing positive electrode (diameter: 12mm).  $Zn||ZnI_2$  pouch cell was assembled by using thin Zn foil (thickness: 20  $\mu m$ , 25  $cm^2$ ) as negative electrode and  $ZnI_2$  self-standing positive electrode (25  $cm^2$ ) and were cycled under a fixed external mechanical pressure applied using a commercial clamping fixture (Guangdong Canrd New Technology Co.). No additional surface treatment was applied to the current collectors prior to electrode fabrication. A commercial glass fiber membrane (Whatman GF/D, pore size: 0.7  $\mu m$ , thickness: 420  $\mu m$ ) was used as the separator for all the cells.

### Electrochemical analyses

Galvanostatic charge/discharge tests of  $Zn||Cu$ ,  $Zn||Zn$ ,  $Zn||ZnI_2$ ,  $Zn||V_6O_{13}$   $Zn||MnO_2$  coin cells and  $Zn||ZnI_2$  pouch cell were performed using the Landt battery test system

(Wuhan LAND Electronic Co.) and NEWARE battery test system (Shenzhen Neware Technology Co.). The Zn plating/stripping CE was measured in Zn||Cu cells by the Aurbach's method and cycle method<sup>38,39</sup>. The processes of Aurbach's method were as follows: First, the plating was deposited, cycled, and formed at 5 mA cm<sup>-2</sup> and 10 mAh cm<sup>-2</sup>; then, the former plating was cycled again at 5 mA cm<sup>-2</sup> and 6 mAh cm<sup>-2</sup>. Finally, the remaining Zn was stripped at 5 mA cm<sup>-2</sup> until the cutoff voltage of 0.5 V was reached.

Electrochemical measurements were performed on a Gamry workstation. Chronoamperometry measurements of Zn||Zn cells were conducted by holding cells at 0.07 V for 0.005 s. Electrochemical impedance spectroscopy (EIS) measurements were carried out in a potentiostatic mode with an AC perturbation amplitude of 10 mV over the frequency range of 100 kHz to 0.01 Hz, using 10 data points per decade. Prior to EIS measurements, the cells were rested at open-circuit voltage (OCV) for 2 h to ensure a quasi-stationary state. During data analysis, obvious outlier points were excluded from the fitting process. The cyclic voltammetry curves of Zn||Zn cells were tested at a scan rate of (2, 6, 10, 14 mV s<sup>-1</sup>), and the EDLC was calculated using  $C = i_c v^{-1}$ , where  $C$  is the capacitance,  $i_c$  is the electric double layer current,  $v$  is the scan rate. The capacitance can be obtained from the slope of the  $i_c$  versus  $v$ . Here,  $i_c$  was defined as half the difference between current during the forward and reverse scans at 0 V, that is  $(i_{0v+} - i_{0v-})/2$ <sup>44</sup>.

The mathematical expressions for classical nucleation models are provided below:

$$3DI: \frac{i}{I_m} = \left( \frac{1.9542t_m}{t} \right)^{0.5} \left[ 1 - \exp\left( -\frac{1.2564t}{t_m} \right) \right] \quad (1)$$

$$3DP: \frac{i}{I_m} = \left( \frac{1.2254t_m}{t} \right)^{0.5} \left[ 1 - \exp\left( -\frac{2.3367t}{t_m} \right)^2 \right] \quad (2)$$

$$2DI: \frac{i}{I_m} = \frac{t}{t_m} \exp\left\{ \frac{1}{2} \left[ 1 - \left( \frac{t}{t_m} \right)^2 \right] \right\} \quad (3)$$

$$2DP: \frac{i}{I_m} = \left( \frac{t}{t_m} \right)^2 \exp\left\{ \frac{2}{3} \left[ 1 - \left( \frac{t}{t_m} \right)^3 \right] \right\} \quad (4)$$

## Characterizations

In situ eQCM was measured through the eQCM system (15M and Interface 1010E,

Gamry) with Au-sputtered 5 MHz quartz substrates (diameter: 14 mm) to monitor the resonance frequency changes of the electrodes. The mass change of the QCM electrode ( $\Delta m$ ) was determined from the resonance frequency shift ( $\Delta f$ ) using the Sauerbrey equation. In the eQCM tests, 2 m ZnSO<sub>4</sub> served as the BE, and the quartz crystal resonator functioned as the working electrode. Platinum wire and Ag/AgCl electrodes were used as the counter and reference electrodes, respectively. The cyclic voltammetry curves were recorded at a scan rate of 50 mV s<sup>-1</sup>, ranging from 0 V to 0.6 V. The QCM test was conducted in three steps: first, a frequency balance was established using a continuously flowing 2 m ZnSO<sub>4</sub> electrolyte; second, the original solution was replaced with various additive electrolytes; and finally, the baseline electrolyte was reintroduced to monitor the frequency change and determine the formation of an adsorption layer. The electrolytes were delivered to the test chamber via a peristaltic pump at a flow rate of 1 mL min<sup>-1</sup>. In the Zn<sup>2+</sup> hydration number test, porous carbon materials (Vulcan XC-72R, Cabot) and PVDF were mixed with NMP at a weight ratio of 9:1. The resulting mixture was uniformly coated onto quartz substrates and dried in a vacuum oven at 80 °C. The coated quartz crystal resonator served as the working electrode, while platinum wire and Ag/AgCl electrodes functioned as the counter and reference electrodes, respectively. CV tests were then performed starting from the open-circuit voltage in the negative direction at a scan rate of 10 mV s<sup>-1</sup> ranging from 0 V to -0.5 V. During cyclic voltammetry, the charge stored or released on the electrode surface can be determined by integrating the current over time (the CV curve). The eQCM data were presented as the relationship between the electrode mass change ( $\Delta m$ ) and the charge passed ( $\Delta Q$ ) during the negative polarization process<sup>45</sup> (red and blue lines in Figures 3d,e).

To establish the theoretical reference for interpreting the eQCM results, the mass-charge responses of bare Zn<sup>2+</sup> and fully hydrated Zn<sup>2+</sup>·6H<sub>2</sub>O were calculated according to Faraday's law (dot and dashed lines in Figures 3d,e). These curves provide the expected  $\Delta m$ - $\Delta Q$  slopes for ions carrying either no hydration water or a full primary hydration shell. By comparing these theoretical slopes with the experimental  $\Delta m$ - $\Delta Q$  relations, the apparent molecular weight ( $M_w$ ) of the interfacial species can be extracted using equation (5)<sup>46</sup>. A deviation of the experimental slope toward higher apparent molecular

weight than either theoretical limit suggests that the interfacial Zn species carry additional coordinated components beyond water.

$$M_{W'} = \frac{nF \cdot \Delta m}{Q} \quad (5)$$

Where  $n$  is the valence state of  $\text{Zn}^{2+}$ ,  $F$  is the Faraday constant ( $96485 \text{ C mol}^{-1}$ ),  $Q$  is the charge amount transferred through the electrode at presumptive 100% coulomb efficiency.

In situ FTIR spectra were acquired using a battery test system (Shenzhen Neware Technology Co.) coupled with a Thermo Fisher Scientific Nicolet iS20 spectrometer. In situ differential electrochemical mass spectrometry was performed using a commercial mass spectrometer (QMS 200 Atmospheric Sampling System, Stanford Research Systems, Inc., USA) connected to a sealed EL-CELL. Prior to testing, the system was purged with pure Ar at  $1 \text{ mL min}^{-1}$  for 12 hours; subsequently, the evolved gas was analyzed during charging and discharging at  $5 \text{ mA cm}^{-2}$  and  $5 \text{ mAh cm}^{-2}$ , respectively. The entire cell setup was maintained in a temperature-controlled environment at  $25 \text{ }^\circ\text{C}$ .

In situ SEIRAS measurements were carried out using a Si ATR prism coated with a chemically deposited Au nanofilm. The prism was pretreated by immersion in HCl:HNO<sub>3</sub> solution (3:1 v/v, 30 min), polishing with 50 nm alumina slurry (10 min), ultrasonic cleaning, oxidation in H<sub>2</sub>SO<sub>4</sub>:H<sub>2</sub>O<sub>2</sub> solution (3:1 v/v, 20 min), and etching in 40 wt% NH<sub>4</sub>F (1 min). For Au deposition, 15 mL of Au plating solution was preheated to  $55 \text{ }^\circ\text{C}$ , mixed with 3 mL of 2% HF, and the treated prism was immersed for 20 min, then rinsed thoroughly with deionized water. The SEIRAS cell employed the Au-coated Si prism as the working electrode and Zn foil as the counter electrode, and spectra were collected in situ during electrochemical cycling.

The interfacial electrochemical behavior of the Zn negative electrode was probed using scanning electrochemical microscopy (SECM, CHI920D). In the SECM experiment, a Cu foil with deposited Zn served as the substrate electrode, while a Pt ultramicroelectrode (UME) with a  $10 \text{ }\mu\text{m}$  radius functioned as the working electrode. All SECM measurements were performed in a  $2 \text{ m ZnSO}_4$  aqueous solution containing

1 mM FcMeOH as the mediator. In SECM feedback imaging, the process involves scanning an ultramicroelectrode at a constant height above the substrate interface, variations in probe current reflect differences in surface topography and electron-transfer activity.

X-ray diffraction patterns (XRD) were recorded on Bruker D2, with Cu K $\alpha$  radiation. Scanning electron microscopy (SEM) images were taken by Thermo Fisher Apero 2s. X-ray photoelectron spectroscopy (XPS) data were required using an A PHI-5702 instrument with Mg K $\alpha$  X-ray source, with a standard binding energy of 284.8 eV for C 1s. Transmission electron microscopy (TEM) images were taken by Talos F200X. XAFS measurements were performed on the RapidXAFS in Anhui Absorption Spectroscopy Analysis Instrument Co, Ltd. The Athena and Artemis modules of the Demeter software package were used to process the extended XAFS (EXAFS) data according to the standard procedures<sup>47</sup>. Wavelet transform was also conducted to analyze EXAFS data<sup>48</sup>.

### **Machine learning selection**

A machine learning approach was adopted for feature selection to identify the most predictive combination of features for our regression model, with Coulombic efficiency designated as the target value. Our dataset encompassed a variety of chemical properties, including dipole moment, dielectric constant, donor number, molecular weight, and others (Table S1). Ridge regression was selected as the base model owing to its effectiveness in mitigating overfitting through L2 regularization. Polynomial features of degree two were generated to capture potential non-linear relationships between features. An exhaustive search across all possible pairs of these features was performed to evaluate their predictive performance, utilizing Leave-One-Out Cross-Validation (LOOCV). The Root Mean Square Error (RMSE) served as the evaluation metric for assessing the predictive accuracy of each feature pair.

### **Calculation methods**

The constant-potential molecular dynamics simulations were executed using LAMMPS software<sup>49</sup>, complemented with the ELECTRODE package. Initial configurations for

the electrode-electrolyte systems were generated utilizing PACKMOL<sup>50</sup> and Moltemplate (<http://www.moltemplate.org/>). The characteristics of H<sub>2</sub>O were depicted using the SPC/E model. For the force-fields parameters of the Zn<sup>2+</sup> and SO<sub>4</sub><sup>2-</sup>, a combination of previous publications<sup>51-53</sup> and RESP2 charges<sup>54,55</sup> was employed. Similarly, the OPLS force field combined with RESP2 charges was utilized for the additives. To address electronic polarization, an electronic continuum correction method was applied with scaled charges (0.75). The simulation protocol began with Langevin dynamics at 500 K for 1 ns to facilitate salt dissociation. Following this, an NVT ensemble run at 500 K for another 1 ns was conducted to further promote salt dissociation. Subsequently, the system underwent an NVT run at 298 K for 5 ns to reach equilibrium without the application of a constant potential. Finally, to simulate the EDL structure under an electric field, an NVT run with a constant potential of 2 V was carried out for 5 ns. The binding energies were determined utilizing the ORCA software package<sup>56</sup>. Geometry optimizations of clusters were conducted at B97-3c level. Single-point energy calculations were then executed at the B3LYP/def2-TZVP level. To adequately address long-range dispersion interactions, Grimme's D3 dispersion correction was applied. Visualization of the EDL structures was accomplished using VESTA<sup>57</sup> and VMD<sup>58</sup>.

### **Figure preparation**

Schematic illustrations (Figs. 1a, 3c,f, 4a, 6d, 7a and S23) were prepared using Microsoft PowerPoint.

## Data availability

Source data are provided with this paper. All computational data file related to descriptor selection, theoretical calculations and simulations have been deposited in “MaterialsCloud” under accession code DOI link<sup>59</sup>.

## Code availability

The code for machine learning in this work have been deposited in “MaterialsCloud” under accession code DOI link<sup>59</sup>.

## References

1. Jiang, L. *et al.* Rational design of anti-freezing electrolytes for extremely low-temperature aqueous batteries. *Nat. Energy* **9**, 839–848 (2024).
2. Li, W., Dahn, J. R. & Wainwright, D. S. Rechargeable lithium batteries with aqueous electrolytes. *Science* **264**, 1115–1118 (1994).
3. Liang, Y. & Yao, Y. Designing modern aqueous batteries. *Nat. Rev. Mater.* **8**, 109–122 (2022).
4. Blanc, L. E., Kundu, D. & Nazar, L. F. Scientific challenges for the implementation of Zn-ion batteries. *Joule* **4**, 771–799 (2020).
5. Ma, L. *et al.* Realizing high zinc reversibility in rechargeable batteries. *Nat. Energy* **5**, 743–749 (2020).

6. Li, C. *et al.* Highly reversible Zn anode with a practical areal capacity enabled by a sustainable electrolyte and superacid interfacial chemistry. *Joule* **6**, 1103–1120 (2022).
7. Li, Y. *et al.* In situ formation of liquid crystal interphase in electrolytes with soft templating effects for aqueous dual-electrode-free batteries. *Nat. Energy* **9**, 1350–1359 (2024).
8. Jiang, H. *et al.* Chloride electrolyte enabled practical zinc metal battery with a near-unity coulombic efficiency. *Nat. Sustain.* **6**, 806–815 (2023).
9. Zhang, B. *et al.* Electrolyte design for reversible zinc metal chemistry. *Nat. Commun.* **16**, 71 (2025).
10. Ming, F. *et al.* Co-Solvent Electrolyte Engineering for Stable Anode-Free Zinc Metal Batteries. *J. Am. Chem. Soc.* **144**, 7160–7170 (2022).
11. Zha, Z. *et al.* Electrolyte design via cation–anion association regulation for high-rate and dendrite-free zinc metal batteries at low temperature. *J. Am. Chem. Soc.* **146**, 31612–31623 (2024).
12. Geng, L. *et al.* Eutectic electrolyte with unique solvation structure for high-performance zinc-ion batteries. *Angew. Chem. Int. Ed.* **61**, e202206717 (2022).
13. Cao, L. *et al.* Solvation structure design for aqueous Zn metal batteries. *J. Am. Chem. Soc.* **142**, 21404–21409 (2020).
14. Cong, J. *et al.* Kinetics compensation mechanism in cosolvent electrolyte strategy for aqueous zinc batteries. *J. Am. Chem. Soc.* **147**, 8607–8617 (2025).

15. Huang, C. *et al.* Stabilizing Zinc Anodes by Regulating the Electrical Double Layer with Saccharin Anions. *Adv. Mater.* **33**, 2100445 (2021).
16. Weng, J. *et al.* Enhancing Zn-metal anode stability: key effects of electrolyte additives on ion-shield-like electrical double layer and stable solid electrolyte interphase. *Adv. Funct. Mater.* **34**, 2314347 (2024).
17. Hu, Y.-S. & Lu, Y. The mystery of electrolyte concentration: from superhigh to ultralow. *ACS Energy Lett.* **5**, 3633–3636 (2020).
18. Xu, J. & Wang, C. Perspective—electrolyte design for aqueous batteries: from ultra-high concentration to low concentration? *J. Electrochem. Soc.* **169**, 030530 (2022).
19. Heo, J., Dong, D., Wang, Z., Chen, F. & Wang, C. Electrolyte design for aqueous Zn batteries. *Joule* **9**, 101844 (2025).
20. Onsager, L. Deviations from ohm's law in weak electrolytes. *J. Chem. Phys.* **2**, 599–615 (1934).
21. Zhu, Z. *et al.* In situ mass spectrometric determination of molecular structural evolution at the solid electrolyte interphase in lithium-ion batteries. *Nano Lett.* **15**, 6170–6176 (2015).
22. Gutmann, V. Empirical parameters for donor and acceptor properties of solvents. *Electrochimica Acta* **21**, 661–670 (1976).
23. Zhou, P., Xiang, Y. & Liu, K. Understanding and applying the donor number of electrolytes in lithium metal batteries. *Energy Environ. Sci.* **17**, 8057–8077 (2024).

24. Xu, J. *et al.* Electrolyte design for Li-ion batteries under extreme operating conditions. *Nature* **614**, 694–700 (2023).
25. Chen, J. *et al.* Design of localized high-concentration electrolytes via donor number. *ACS Energy Lett.* **8**, 1723–1734 (2023).
26. Choi, I. R. *et al.* Asymmetric ether solvents for high-rate lithium metal batteries. *Nat. Energy* **10**, 365–379 (2025).
27. Duan, A. *et al.* In situ monitoring of dynamic adsorption-induced interfacial buffering toward highly stable zinc metal batteries. *Adv. Energy Mater.* 2404693 (2025).
28. Jensen, K., Kim, K. & Zettl, A. An atomic-resolution nanomechanical mass sensor. *Nat. Nanotechnol.* **3**, 533–537 (2008).
29. Liu, T. *et al.* In situ quantification of interphasial chemistry in Li-ion battery. *Nat. Nanotechnol.* **14**, 50–56 (2019).
30. Yu, X. *et al.* Unlocking dynamic solvation chemistry and hydrogen evolution mechanism in aqueous zinc batteries. *J. Am. Chem. Soc.* **146**, 17103–17113 (2024).
31. Yu, X. *et al.* Deciphering multi-dimensional interfacial mechanisms via organic cosolvent engineering for sustainable zinc metal batteries. *Nat. Commun.* **16**, 3820 (2025).
32. Cheng, H. *et al.* Emerging era of electrolyte solvation structure and interfacial model in batteries. *ACS Energy Lett.* **7**, 490–513 (2022).
33. Whittingham, M. S. Electrical energy storage and intercalation chemistry. *Science*

- 192**, 1126–1127 (1976).
34. Zhao, J. *et al.* Epitaxy Orientation and Kinetics Diagnosis for Zinc Electrodeposition. *ACS Nano* **19**, 736–747 (2025).
35. Scharifker, B. & Hills, G. Theoretical and experimental studies of multiple nucleation. *Electrochimica Acta* **28**, 879–889 (1983).
36. Bewick, A., Fleischmann, M. & Thirsk, H. R. Kinetics of the electrocrystallization of thin films of calomel. *Trans. Faraday Soc.* **58**, 2200 (1962).
37. Yao, Y.-X. *et al.* Nucleation and growth mode of solid electrolyte interphase in Li-ion batteries. *J. Am. Chem. Soc.* **145**, 8001–8006 (2023).
38. Ma, L. *et al.* Critical factors dictating reversibility of the zinc metal anode. *Energy Environ. Mater.* **3**, 516–521 (2020).
39. Aurbach, D., Daroux, M., Faguy, P. & Yeager, E. The electrochemistry of noble metal electrodes in aprotic organic solvents containing lithium salts. *J. Electroanal. Chem. Interfacial Electrochem.* **297**, 225–244 (1991).
40. Xing, Z. *et al.* Zincophilic electrode interphase with appended proton reservoir ability stabilizes Zn metal anodes. *Angew. Chem. Int. Ed.* **62**, e202215324 (2023).
41. Li, M. *et al.* Strategically modulating proton activity and electric double layer adsorption for innovative all-vanadium aqueous  $Mn^{2+}$ /proton hybrid batteries. *Adv. Mater.* **36**, 2407233 (2024).
42. Wu, H. *et al.* Aqueous zinc–iodine pouch cells with long cycling life and low self-discharge. *J. Am. Chem. Soc.* **146**, 16601–16608 (2024).

43. Shan, L. *et al.* Highly reversible phase transition endows  $V_6O_{13}$  with enhanced performance as aqueous zinc-ion battery cathode. *Energy Technol.* **7**, 1900022 (2019).
44. Li, T. C. *et al.* Interfacial molecule engineering for reversible Zn electrochemistry. *ACS Energy Lett.* **8**, 3258–3268 (2023).
45. Tsai, W.-Y., Taberna, P.-L. & Simon, P. Electrochemical Quartz Crystal Microbalance (EQCM) Study of Ion Dynamics in Nanoporous Carbons. *J. Am. Chem. Soc.* **136**, 8722–8728 (2014).
46. Deng, J. *et al.* Accelerating ion desolvation via bioinspired ion channel design in nonconcentrated aqueous electrolytes. *J. Am. Chem. Soc.* **147**, 5943–5954 (2025).
47. Ravel, B. & Newville, M. *ATHENA*, *ARTEMIS*, *HEPHAESTUS*: data analysis for X-ray absorption spectroscopy using *IFEFFIT*. *J. Synchrotron Radiat.* **12**, 537–541 (2005).
48. Funke, H., Scheinost, A. C. & Chukalina, M. Wavelet analysis of extended x-ray absorption fine structure data. *Phys. Rev. B* **71**, 94110 (2005).
49. Plimpton, S. Fast parallel algorithms for short-range molecular dynamics. *J. Comput. Phys.* **117**, 1–19 (1995).
50. Martínez, L., Andrade, R., Birgin, E. G. & Martínez, J. M. PACKMOL: a package for building initial configurations for molecular dynamics simulations. *J. Comput. Chem.* **30**, 2157–2164 (2009).
51. Jorgensen, W. L., Maxwell, D. S. & Tirado-Rives, J. Development and testing of

- the OPLS all-atom force field on conformational energetics and properties of organic liquids. *J. Am. Chem. Soc.* **118**, 11225–11236 (1996).
52. Jang, Y. H. *et al.* The MSXX Force Field for the Barium Sulfate– Water Interface. *J. Phys. Chem. B* **106**, 9951–9966 (2002).
53. Canongia Lopes, J. N. & Pádua, A. A. Molecular force field for ionic liquids composed of triflate or bistriflylimide anions. *J. Phys. Chem. B* **108**, 16893–16898 (2004).
54. Bayly, C. I., Cieplak, P., Cornell, W. & Kollman, P. A. A well-behaved electrostatic potential based method using charge restraints for deriving atomic charges: the RESP model. *J. Phys. Chem.* **97**, 10269–10280 (1993).
55. Lu, T. & Chen, F. Multiwfn: A multifunctional wavefunction analyzer. *J. Comput. Chem.* **33**, 580–592 (2012).
56. Neese, F. The ORCA program system. *WIREs Comput. Mol. Sci.* **2**, 73–78 (2012).
57. Momma, K. & Izumi, F. VESTA 3 for three-dimensional visualization of crystal, volumetric and morphology data. *J. Appl. Crystallogr.* **44**, 1272–1276 (2011).
58. Humphrey, W., Dalke, A. & Schulten, K. VMD: visual molecular dynamics. *J. Mol. Graph.* **14**, 33–38 (1996).
59. Yang, M. *et al.* Electric-Field-Reinforced Affinitive Electrolytes for Highly Reversible Aqueous Zinc Metal Batteries. *Mater. Cloud Arch.* <https://doi.org/10.24435/materialscloud:tk-qk> (2026).

## Acknowledgments

B.Z. acknowledges the financial support from National Natural Science Foundation of China (No. 22509023) and the Sichuan Science and Technology Program (No. 2025ZNSFSC0964). W.S. acknowledges the National Natural Science Foundation of China (Nos. U2330119 and 52302221). H.Z.W. acknowledges the support from National Natural Science Foundation of China (No. 52272198). The authors also acknowledge the support of computational resources provided by the High-performance Computing Platform of UESTC.

## Author contributions

W.S., H.Z.W., H.W., B.Z., and M.Y. conceived the idea and designed the experiments. M.Y. and B.Z. performed materials characterizations and electrochemical measurements with assistance from A.D., S.L., L.Y.G., J.Q.W., Y.X.Z., Y.F., X.H., Y.Y.T. and J.Y. B.Z. performed the MD simulations, DFT calculations, and machine learning analyses. M.Y. and B.Z. co-wrote the paper. All authors discussed the results and commented on the manuscript.

## Competing interests

The authors declare that a patent application related to the electrolyte formulation described in this work has been filed (Patent No. 2025108426814).

## Figure Captions

**Figure 1. Design concept of ERAE.** (a) Schematic illustration of the interfacial behavior of shielding, inert and affinitive additives at the Zn interface under an applied

electric field. (b) Root mean square error (RMSE) matrix obtained from leave-one-out cross-validation (LOOCV) analysis of ridge-regression-based feature-pair prediction. Each cell shows the prediction error between two descriptors. Values greater than 2.3 are displayed in white to prevent extreme entries from dominating the color scale. Full descriptor names are listed in Table S2. (c) Plot of donor number (DN) versus dipole moment ( $\mu$ ) for 12 additives, delineating EWSE (I), EWIE (II) and ERAE (III) regions. The area of each circle represents the Zn||Zn symmetric cell life span at 60% depth of discharge (DOD), and stars indicate potential candidates. All electrochemical data were obtained at 25 °C. Source data are provided as a Source Data file.

**Figure 2. Interfacial dynamics of the electric double layer (EDL).** (a) Electrochemical quartz crystal microbalance (eQCM)-measured dynamic mass variation ( $\Delta m$ ) on an Au QCM electrode in 2 m ZnSO<sub>4</sub> (BE) and the ERAE(DMU). (b) Correlation between electrode mass variation and applied potential for 15 electrolytes. The color of each data point represents the Pearson correlation coefficient ( $r$ ), and the circle size denotes the amplitude ratio (AR) extracted from the periodic mass response. The BE (H<sub>2</sub>O) serves as the reference electrolyte. (c) Hydrogen (H<sub>2</sub>) evolution rate measured by differential electrochemical mass spectrometry during Zn plating/stripping in a Zn||Cu asymmetric cell using the ERAE(DMU) and the BE. (d, e) Molecular dynamics (MD) simulation snapshots of the EDL structure at the Zn interface for ERAE(DMU) (d) and EWIE(SL) (e) under an applied bias. (f) Quantitative comparison of additive number density in the EDL with and without an applied electric field based on MD simulations. All electrochemical data were obtained at 25 °C. Source data are provided as a Source Data file.

**Figure 3. Interfacial Solvation Dynamics.** (a, b) Relative absorbance evolution,  $A(t_x)$ - $A(t_0)$  during Zn plating and stripping measured by in situ attenuated total reflectance Fourier transform infrared (ATR-FTIR) spectroscopy in Zn||Cu asymmetric cells with ERAE(DMU) (a), and the BE (b). (c) Schematic of ERAE(DMU) regulation mechanism for organic-rich interface. (d, e) Electric-field-induced modification of

interfacial  $\text{Zn}^{2+}$  hydration. Coordinated species determined from  $\Delta m-\Delta Q$  analysis for ERAE(DMU) (d), and the BE (e). (f) Solvated  $\text{Zn}^{2+}$  show organic exclusion in ERAE(DMU) and water penetration in BE within carbon black. (g) Correlation between  $\text{Zn}^{2+}$  binding energy and electric-field response of additives. (h) Number of additive molecules in the  $\text{Zn}^{2+}$  solvation shell from MD simulations under field-free and electric field conditions. All electrochemical data were obtained at 25 °C. Source data are provided as a Source Data file.

**Figure 4. Deposition morphology analysis.** Unless otherwise specified, all Zn deposition experiments and the corresponding ex situ morphology characterizations in this figure were conducted at a current density of 5 mA cm<sup>-2</sup> with a deposited capacity of 5 mAh cm<sup>-2</sup>. (a) Schematic illustration of scanning electrochemical microscopy (SECM) setup. (b, c) SECM feedback current maps of Zn deposition on Cu substrates in the ERAE(DMU) (b), and the BE (c). (d) In situ optical microscopy tracking Zn plating over 1h at a current density of 5 mA cm<sup>-2</sup>. (e) Confocal scanning microscopy (CLSM) images of Zn surfaces after deposition. (f) SEM images of Zn deposits formed in the ERAE(DMU) and BE. (g) Normalized current–time transients at different applied potentials, compared with classical nucleation models. 2DI, 2DP, 3DI and 3DP denote instantaneous and progressive two-dimensional and three-dimensional nucleation models, respectively. All electrochemical data were obtained at 25 °C. Source data are provided as a Source Data file.

**Figure 5. Electrochemical performance of half cells.** (a) Zn plating/stripping performance of Zn||Zn symmetric cells at 30, 60, 70, and 80% depth of discharge (DOD). Here, 100% DOD is defined as the complete consumption of a 10 μm Zn foil, corresponding to an areal capacity of 5.85 mAh cm<sup>-2</sup>. Accordingly, 30%, 60%, 70% and 80% DOD were achieved using current densities of 1.75, 3.51, 4.1, 4.68 mAh cm<sup>-2</sup>, respectively. (b) Zn plating/stripping performance of Zn||Zn symmetric cells at different current densities, with the cutoff capacity defined by 100% DOD (5.85 mAh cm<sup>-2</sup>). (c) Average coulombic efficiency of the two electrolytes assessed via Aurbach's method.

(d) Comparison of DOD, cumulative plating capacity (CPC) and normalized electrolyte cost relative to representative previous studies, based on simplified post hoc estimates. The source of the literature data are summarized in Supplementary Tables S3-S5. All electrochemical data were obtained at 25 °C. Source data are provided as a Source Data file.

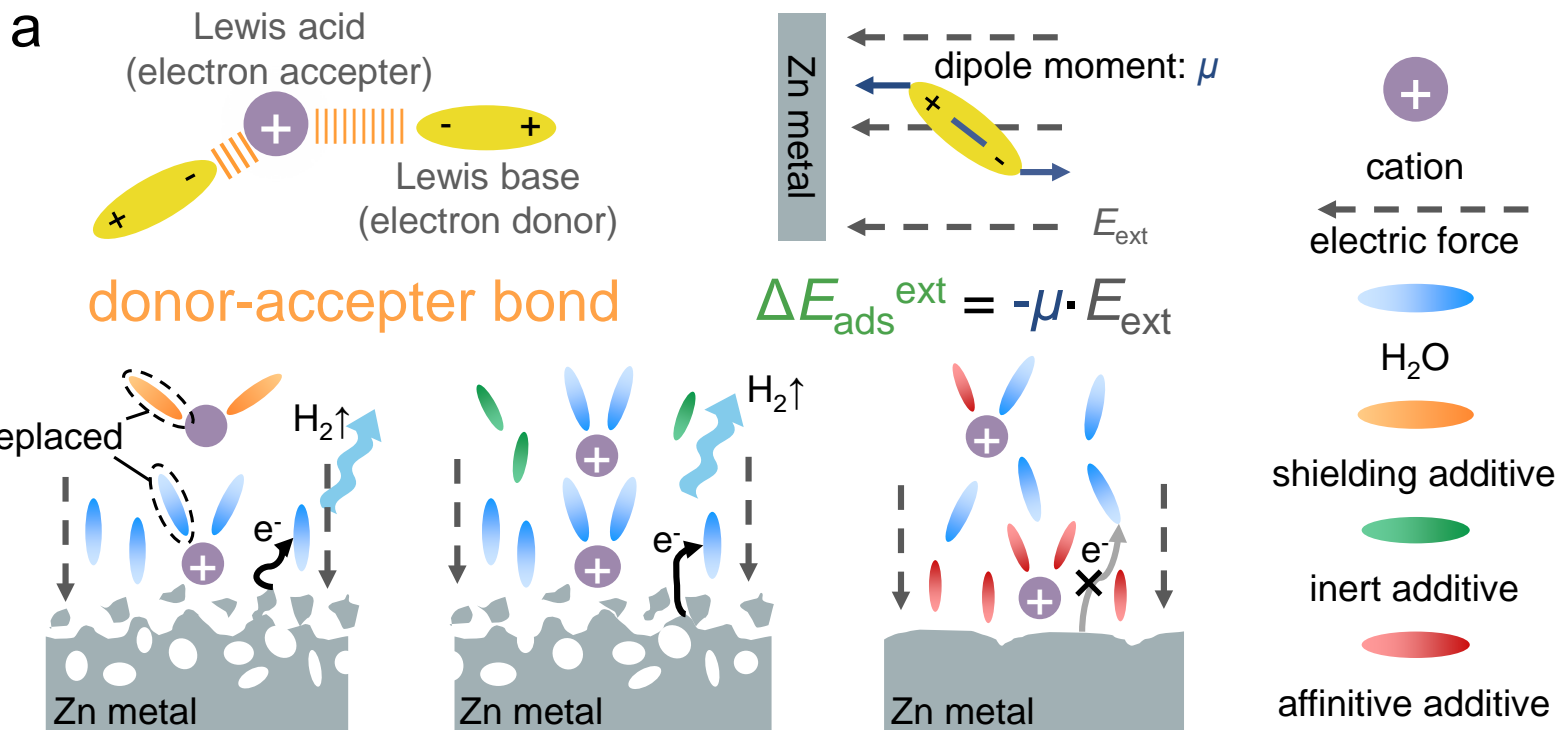
**Figure 6. Full-cell electrochemical performance.** (a) Cycling stability and CE of 10  $\mu\text{m}$  Zn ||  $\text{V}_6\text{O}_{13}$  coin cells at 0.3 A  $\text{g}^{-1}$  (17.7 mg  $\text{cm}^{-2}$ ). (b) Cycling performance of 10  $\mu\text{m}$  Zn||ZnI<sub>2</sub> coin cells at 1 C and 4 C with 60-80  $\mu\text{L}$  electrolyte. (c) Selected galvanostatic charge-discharge (GCD) profiles of Zn||ZnI<sub>2</sub> pouch cells. (d) Cycling stability and CE of 20  $\mu\text{m}$  Zn || ZnI<sub>2</sub> pouch cells (25  $\text{cm}^2$ ) at 4 mA  $\text{cm}^{-2}$ . All electrochemical data were obtained at 25 °C. Source data are provided as a Source Data file.

**Figure 7. Data-driven discovery of electric-field affinitive additives.** (a) Schematic of the multistage filtering pipeline used to identify promising electrolyte additives from a large molecular database. (b) Zn plating/stripping performance of Zn||Zn symmetric cells at 60% depth of discharge (DOD) using two selected additives from the final candidate pool. All electrochemical data were obtained at 25 °C. Source data are provided as a Source Data file.

### Editorial Summary

Aqueous zinc batteries suffer from poor reversibility due to interfacial instability. Here, the authors propose an electric field-responsive electrolyte design that modulates zinc-ion solvation and interfacial chemistry, leading to uniform deposition and extended cycling stability.

**Peer review information:** *Nature Communications* thanks Dejian Dong, Xiaoli Zhao and the other, anonymous, reviewer(s) for their contribution to the peer review of this work. A peer review file is available.

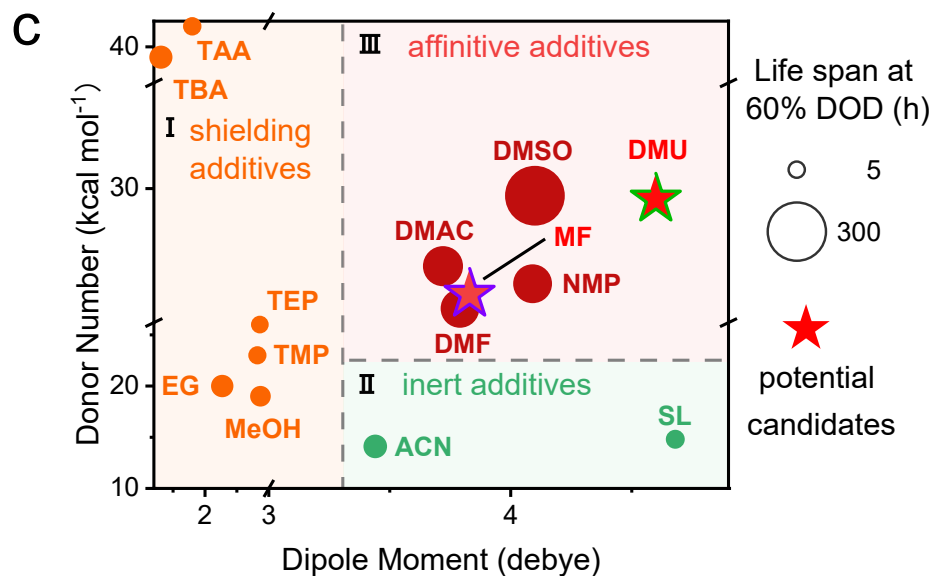


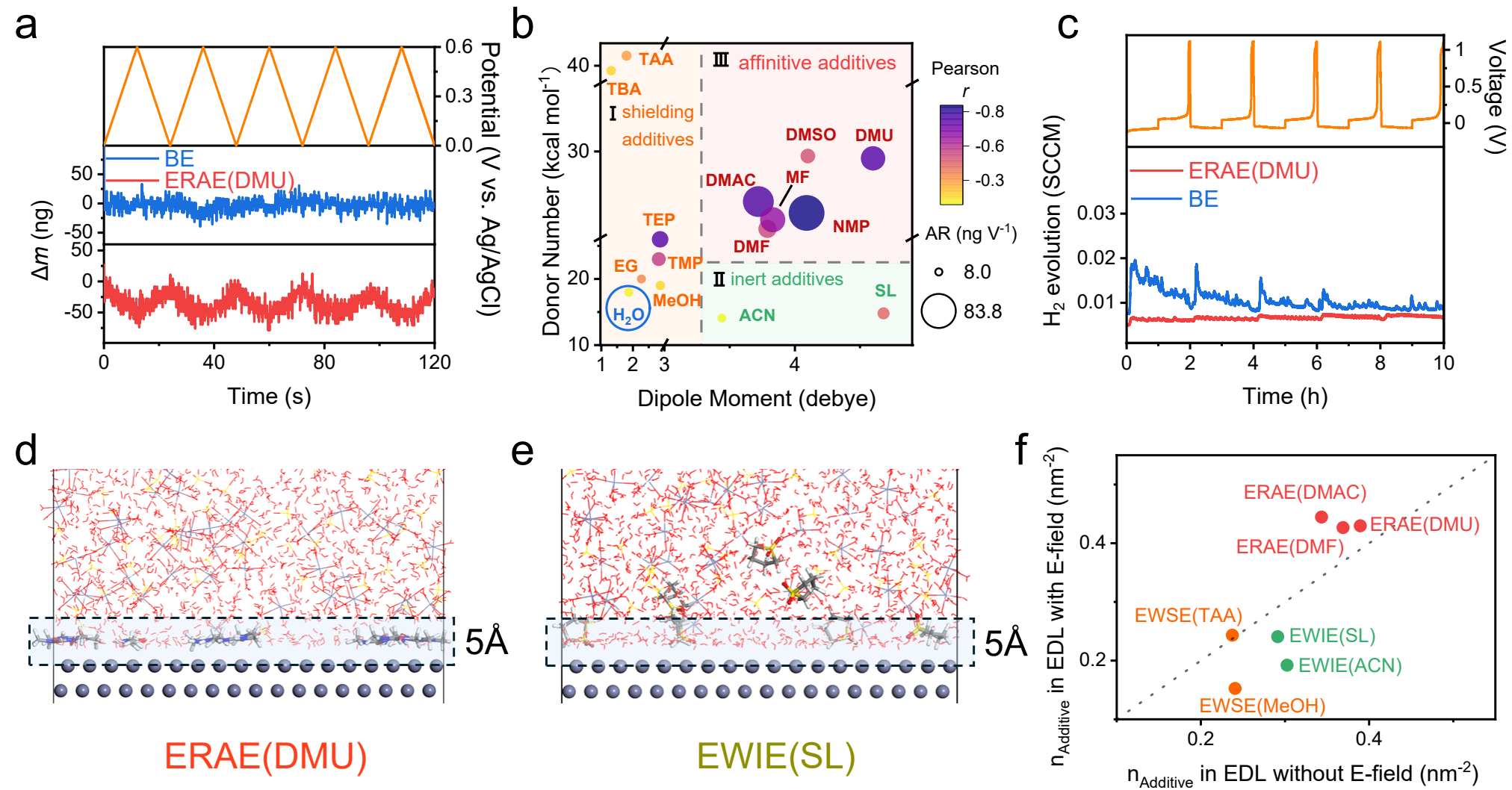
working condition weakened

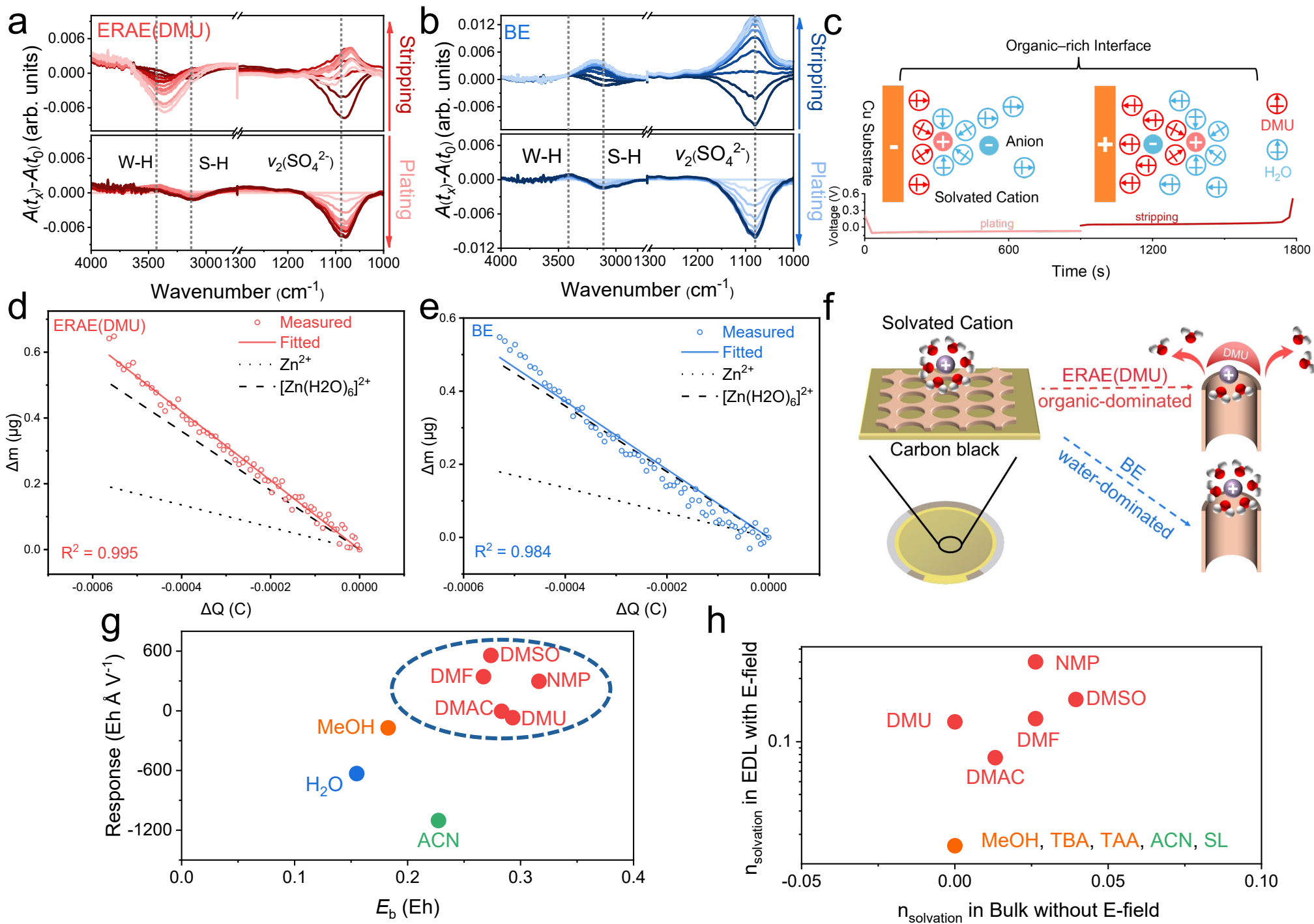
working condition reinforced

**b**

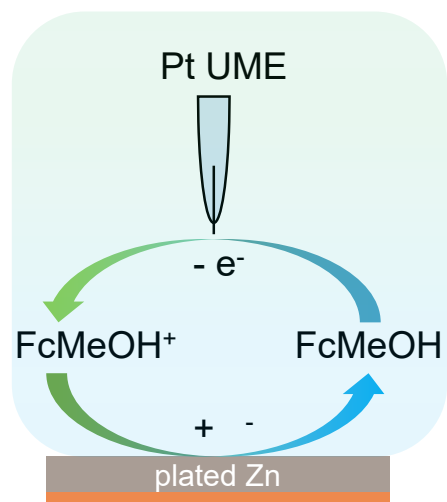
hbac	-1.415	8.684	1.594	2.058	1.972	2.171	2.003	2.137	2.094	2.052	2.291	--	RMSE
hbdc	-1.533	8.160	1.637	2.104	2.176	2.230	2.169	1.889	2.280	2.054	--	2.291	
hac	-1.274	8.379	1.695	2.028	2.021	2.178	1.933	2.118	2.137	--	2.054	2.052	
tpsa	-1.408	9.024	1.661	2.139	2.036	2.287	2.021	2.249	--	2.137	2.280	2.094	
et	-1.289	8.740	1.836	2.131	2.267	2.284	2.204	--	2.249	2.118	1.889	2.137	
bp	-1.438	8.499	1.781	1.924	2.166	2.190	--	2.204	2.021	1.933	2.169	2.003	
mp	-1.289	9.024	1.863	2.202	2.251	--	2.190	2.284	2.287	2.178	2.230	2.171	
pho	-1.439	8.675	1.791	2.003	--	2.251	2.166	2.267	2.036	2.021	2.176	1.972	
mw	-1.271	8.342	1.666	--	2.003	2.202	1.924	2.131	2.139	2.028	2.104	2.058	
dn	-1.234	7.339	--	1.666	1.791	1.863	1.781	1.836	1.661	1.695	1.637	1.594	
dc	-5.297	--	7.339	8.342	8.675	9.024	8.499	8.740	9.024	8.379	8.160	8.684	
dm	--	5.297	1.234	1.271	1.439	1.289	1.438	1.289	1.408	1.274	1.533	1.415	
	dm	dc	dn	mw	pho	mp	bp	et	tpsa	hac	hbdc	hbac	



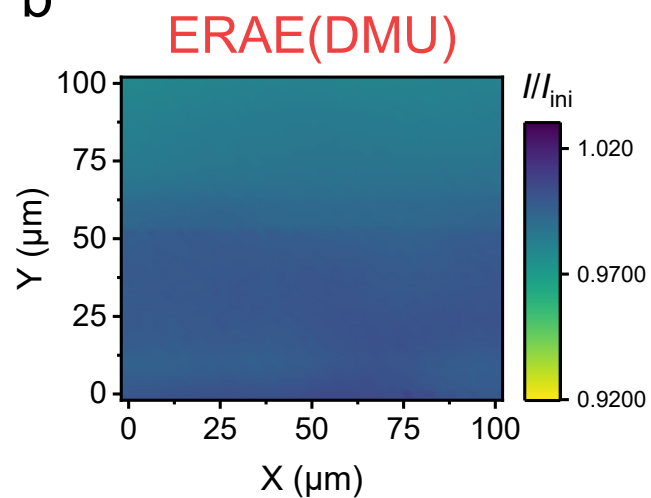




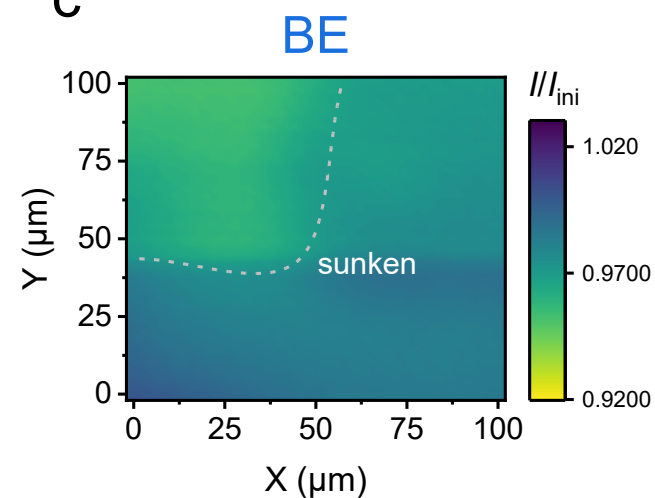
a



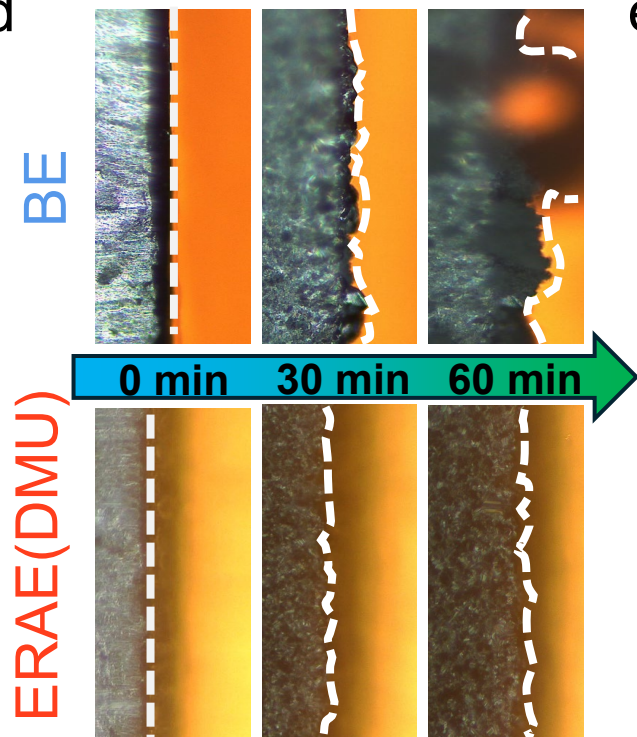
b



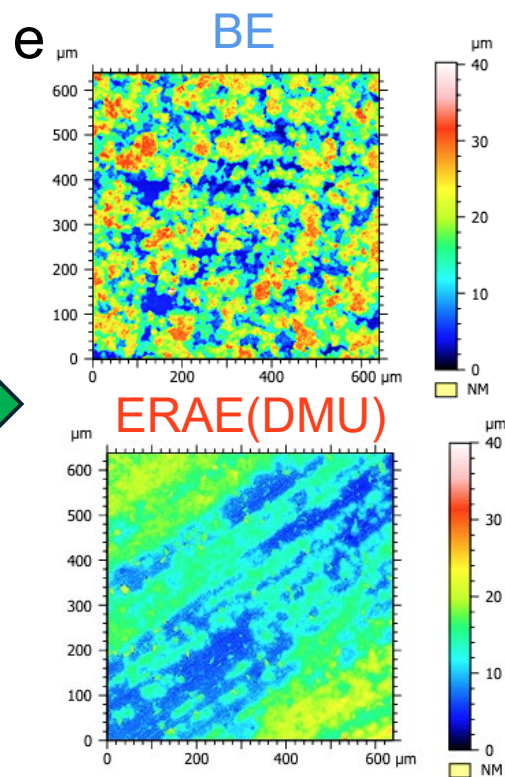
c



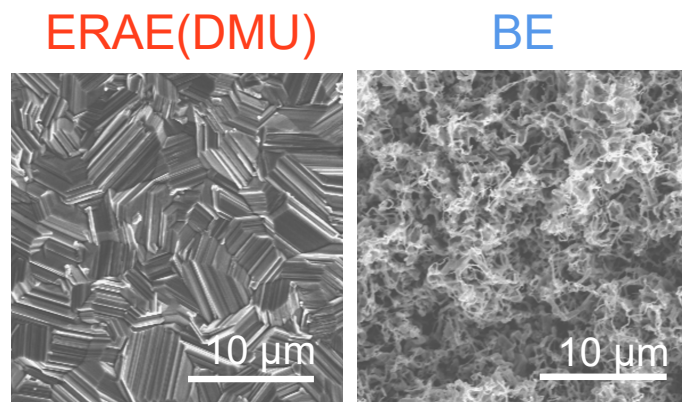
d



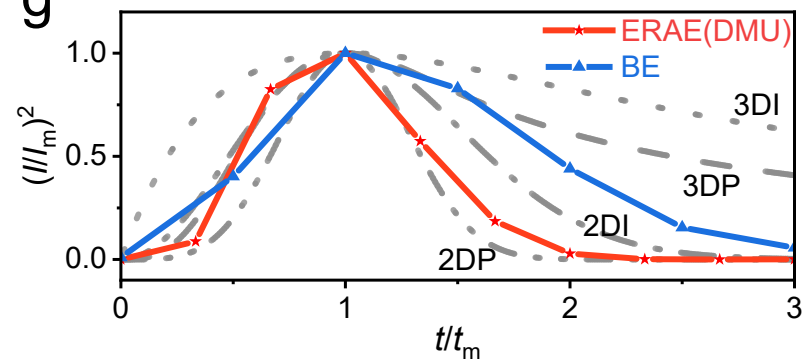
e

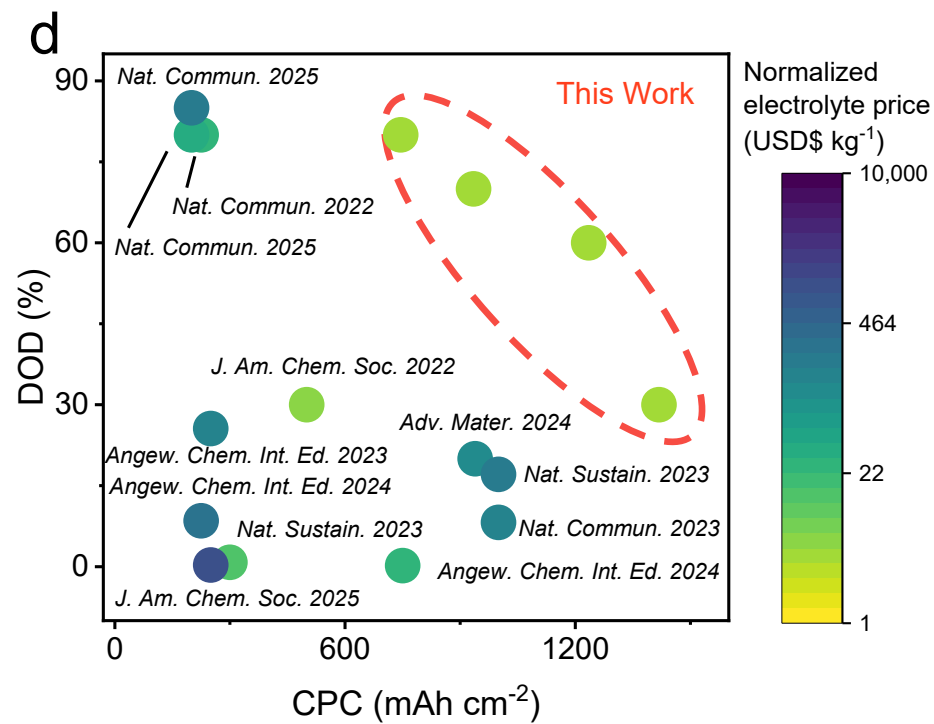
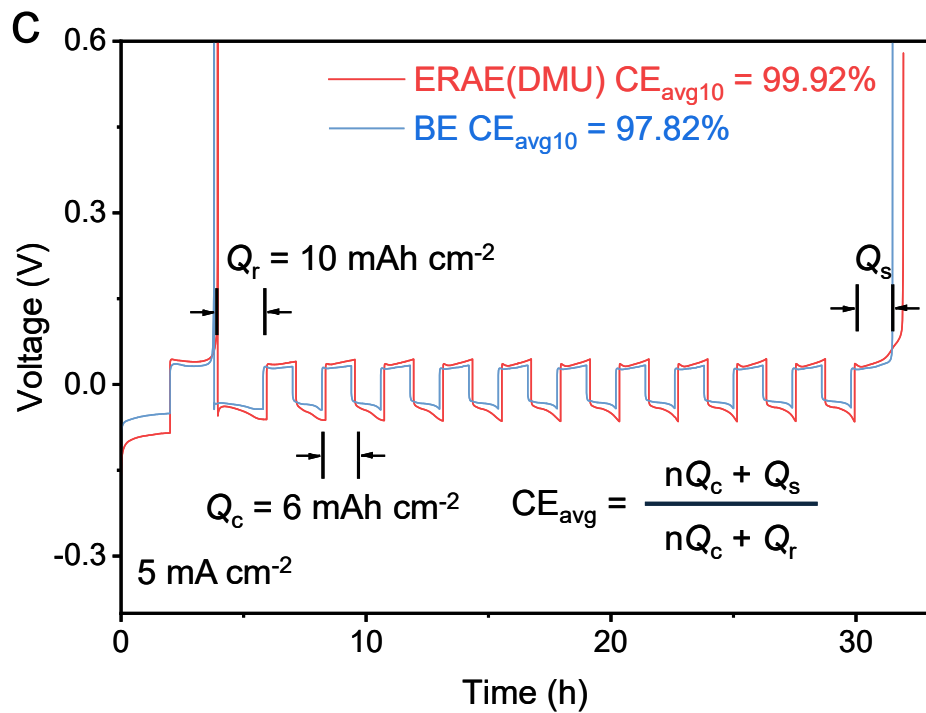
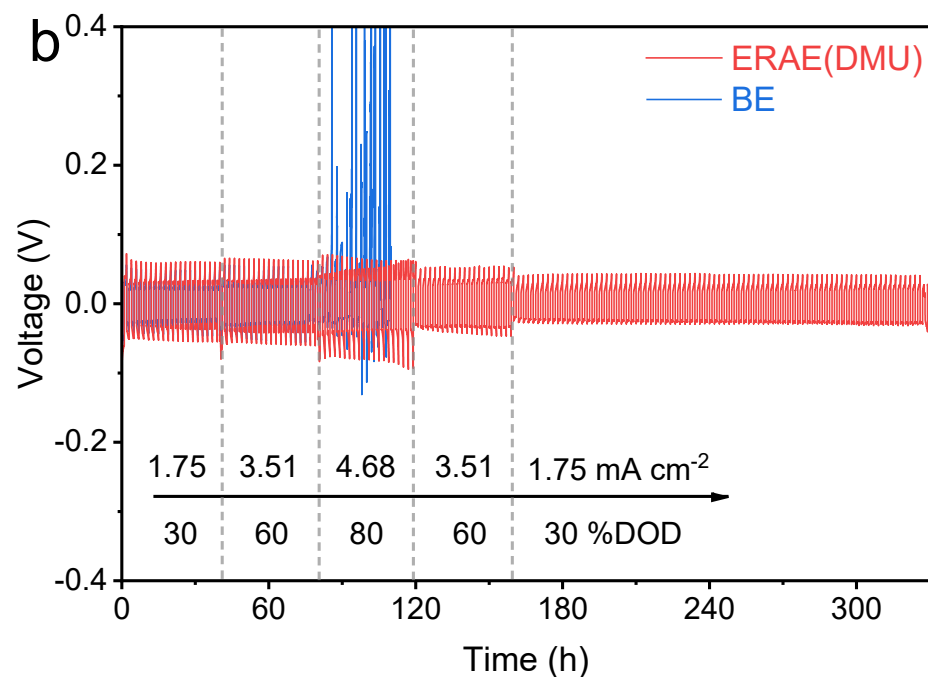
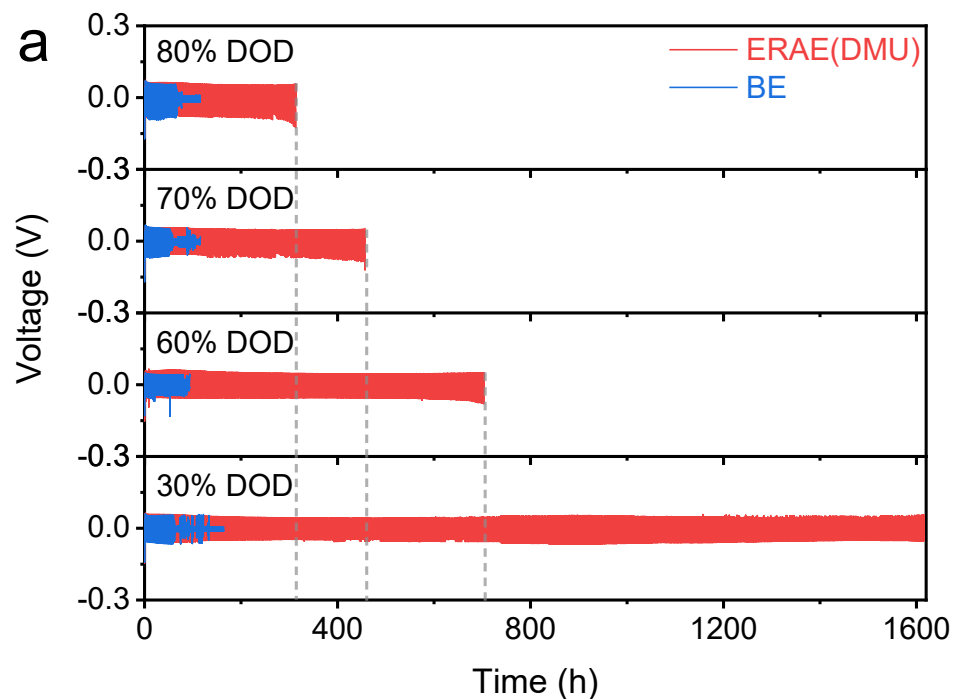


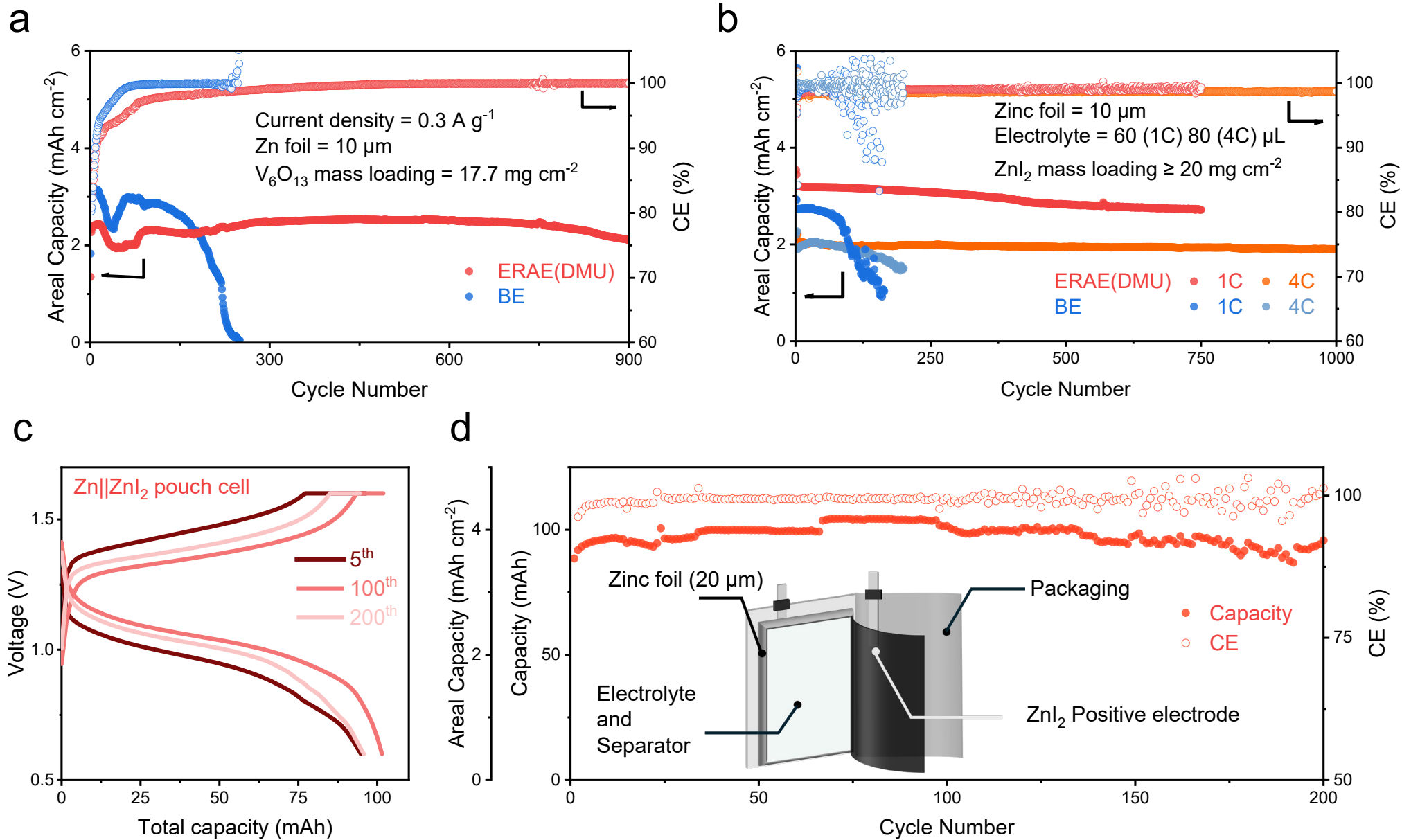
f



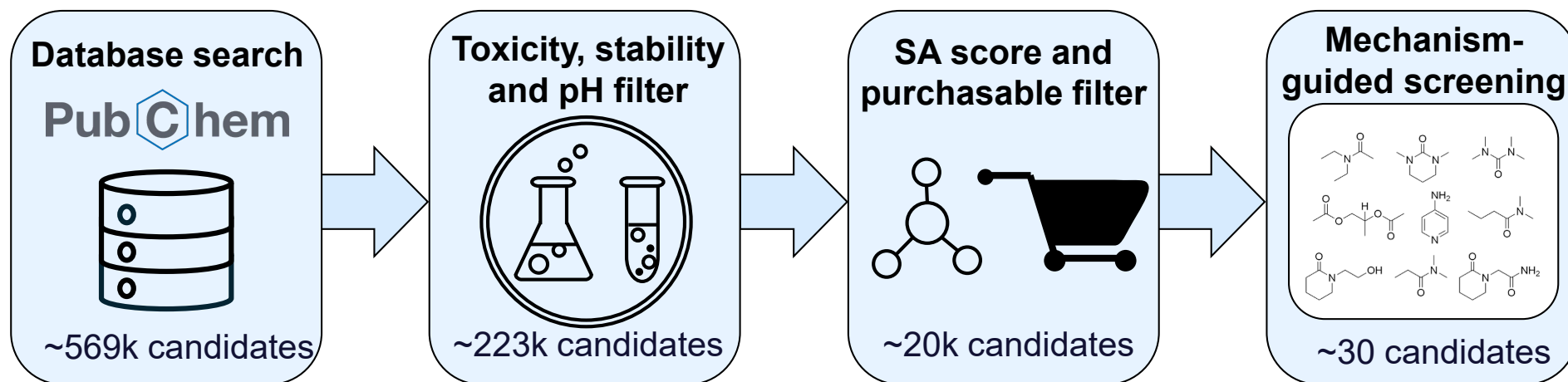
g







a



b

